Triple-Band Circular Ring Monopole Antenna for RF Power Harvesting Applications

Joseph Mari Mebara Mbida[1], Guy Ayissi Eyebe[1, 2], Ghanshyam Singh[3], Clément Mbinack[1], Mohamed Njianga Yende[1]

[1] Department of Physics, Faculty of Sciences, University of Yaounde I, Yaounde, Cameroon

[2] Electrical and Computing Engineering Department, Université du Québec à Trois-Rivieres; Canada

[3] Department of Electronics and Communication Engineering, Feroze Gandhi Institute of Engineering and Technology, Raebareli, India

Corresponding author: Ghanshyam Singh (e-mail: ghanshyamtanu@rediffmail.com).

ABSTRACT This paper presents a simple and efficient approach for an antenna design and construction based on an I-shaped slot-loaded triple wideband microstrip monopole antenna with novel radio frequency (RF) power/energy harvesting capability. The proposed antenna takes advantage of circular ring shape properties, loaded with an I-shaped slot with degraded ground structure (DGS) to improve the input performances of the conventional planar circular microstrip patch antenna (C-patch). Input impedance and magnetic field radiation pattern are calculated using the electromagnetic theory of transmission line in traveling waves and resonant cavity TE_{11} field mode, respectively. The proposed antenna is configured on thin lossy substrate material RO4003C of volume 64.800×57.000×1.524 (in mm^3), relative dielectric permittivity ε_r = 3.55, and numerically investigated using CST MWS. The prototype of the proposed antenna has been fabricated and tested. The experimental results show that the fabricated antenna exhibits an impressive 142% (2.98-11.11 GHz), 21.3% (11.54-14.42 GHz), and 19.6% (15.78-19.44 GHz) fractional bandwidth (FBW) for the resonant frequency of 5.73, 13.55, and 18.69 GHz respectively and peak gain of 4.2 dBi at the frequency of 5.8 GHz. Experimentally, the proposed antenna can be used in multiple applications like 2.4 GHz (2.401-2.495 GHz) Wi-Fi band/5 GHz (5.170-5.875 GHz) WLAN band/(3.1-10.6 GHz) US UWB at the view of the achieved lower band, FR3 6G operation regarding the obtained middle/intermediate band, and the future wireless and millimeter-wave communication systems according to the obtained upper band.

INDEX TERMS Input Impedance, Magnetic field radiation pattern, Multiband, RF power/energy harvesting.

I. INTRODUCTION

NOWADAYS, there is a growing trend toward using low-power wireless equipment [1, 2]. Wireless technologies are rapidly becoming an integral part of our lives due to their undisputed usefulness and advantages of facilitating our daily habits. The proliferation and the use of this technology in an urban area by authorities and civilians to improve the quality of urban services, increase the economy, maintain security and share information make this area a smart city and a pure source of radio frequency energy as depicted in Fig. 1A. In the context of smart city transportation systems like motorcycle, bicycle, car, auto, bus, train and all other wireless terminals can use RF energy harvesting technology to recharge their own energy source by converting the received EM power to DC voltage using the developed module. The smart city concept integrates information, communication technologies, and multiple physical devices connected to the network to optimize urban services and improve citizen lives. However, the main problem wich such integration is the energy consumption. This concern about the energy supply of connected equipment has led to several lines of research which have resulted in the improvement of batteries and the development of innovative continuous recharging technologies (thermal, magnetic and electromagnetic energy recovery) [3, 4]. The energy sources used include wind, vibration, magnetic wave, electromagnetic waves, and solar energy [5]. One other source susceptible to be used is the novel radio frequency (RF) wave [6].

RF wave is an electromagnetic wave originating from the displacement of a transmitter's own charge in a specific frequency band (X-band, VHF, UWB, S-band, SHF, DBS band) [1, 2, 7]. The RF energy source is clean and compatible with Wi-Fi, WiMAX, and FM networks because of the low power emitted [8-10]. Its recovery and conversion are done with the help of an electronic system called rectenna whose operating block-diagram is shown in Fig. 1B with the mathematical expression elaborated to evaluate the maximum harvested DC voltage as [1]

$$\eta(\%) = \frac{P_{out}}{P_{RF}} = \frac{V_{DC}^2}{R_{load}} \cdot \frac{100}{P_{RF}} \quad (1)$$

that yields

$$V_{DC} = \left(R_{load} \cdot \eta(\%) \cdot \frac{P_{RF}}{100} \right)^{\frac{1}{2}} \quad (2)$$

Where R_{load} is the load resistance, P_{RF} is the amplified RF power of the received/emitted antenna, η the target efficiency, and V_{DC} is the maximum harvested DC voltage.

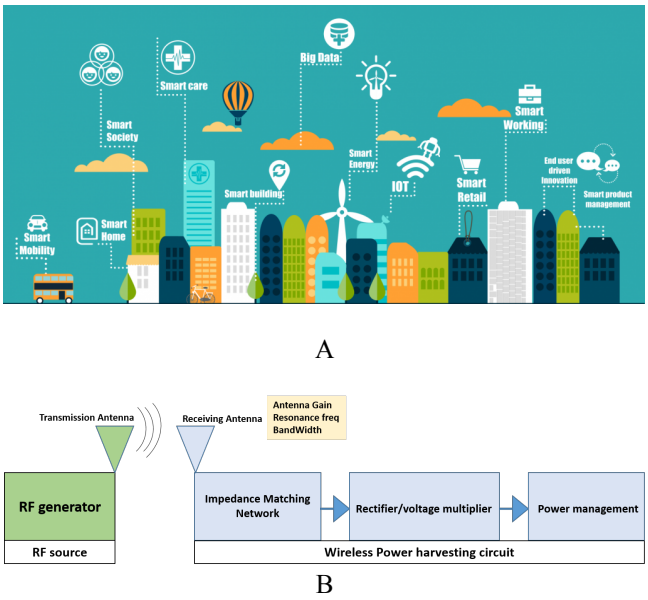

FIGURE 1. Conceptual study. A) Smart city, B) block-diagram of the RF power harvesting system.

This system uses conventional bandwidths of RF power recovery with minimal harvested energy of about $2\mu W/cm^2$ [1, 2, 11]. In such a system the module allocated to the receiver antenna is very important because it is the tool that collects the RF wave [12, 13]. Therefore, several antenna models have been used in this passive recovery system, such as rectangular (R-)/circular (C-)/elliptical (E-) microstrip patch antenna [14-16]. However, the R-/C-/E-patch antenna suffers from mismatch, single narrow bandwidth, and linear polarization (LP). Some researchers have devoted their energy to improve microstrip patch antenna performances [17, 18].

Two semi-circular monopole antenna components with a novel groundbreaking approach by combining MIMO technology with RF radio frequency energy harvesting are introduced in [6]. In [19], two compact planar ring slots printed on a Rogers Duroid 5880 with two resonant passbands at 2.45 GHz and 5.8 GHz for the realization of a rectenna are proposed. In [20], an RF energy harvesting system based on a dual-band folded dipole antenna with a length of only 36.6% of the half-wave dipole antenna operating at 915 MHz and 2.45 GHz is proposed. A multi-band monopole antenna with L-shaped stubs printed on FR-4 substrate operating at five bandwidths (GPS band, DSC band, ISM band, Wi-Fi band, and WiMAX band) for radio frequency energy harvesting applications is demonstrated in [21]. In [22], a triple-band single layer rectifying E-shaped antenna printed on FR-4 substrate material for RF energy harvesting applications operating at the LoRaWAN band, GSM-1800 band, and UMTS-2100 band is proposed. The article [23] presents an ultra-lightweight and compact multiband rectenna, fabricated on a paper substrate, designed for RF energy harvesting in next-generation Long Term Evolution (LTE) bands (0.79–0.96 GHz; 1.71–2.17 GHz; and 2.5–2.69 GHz). The rectenna integrates an antenna and a rectifier optimized to operate in these bands, with an RF-to-DC conversion efficiency ranging from 5% to 16% for an input power of -20 dBm, and reaching 11% to 30% at -15 dBm. The design is based on a nested annular slot topology, enabling seamless integration between the antenna and the rectifier. The article [24] presents a tri-band rectenna based on a microstrip patch antenna integrated with a rectifier circuit, designed for RF energy harvesting systems. The rectenna is particularly suited for powering low-power wireless sensor networks with rechargeable battery supplies. The antenna operates at three frequency bands: 2.4–2.5 GHz and 5-5.1 GHz (WLAN bands) as well as 4-4.15 GHz (C band). The rectenna is modeled using the Ansoft HFSS simulator and fabricated on a low-cost FR-4 substrate. The rectenna's performance is measured in an anechoic chamber and shows good correlation with simulated results. The rectenna achieves a DC output voltage of 298 mV in the operational bands. The article [25] presents a dual-polarized multiband rectenna designed for RF energy harvesting in the C-band (4–8 GHz). The rectenna consists of a multiband microstrip patch antenna and a voltage doubler rectifier, optimized to efficiently convert ambient RF energy into DC power. The antenna is designed to operate at six frequency bands (4.75 GHz, 5.42 GHz, 5.76 GHz, 6.4 GHz, 6.9 GHz, and 7.61 GHz) and offers circular polarization at three of these bands (5.42 GHz, 6.9 GHz, and 7.61 GHz). The rectenna achieves a maximum RF-to-DC conversion efficiency of 84% at 5.76 GHz with an input power of 15 dBm.

In this work, a compact rectenna module-based I-shaped slot-loaded triple-band circular ring monopole patch antenna (CRMPA) printed on a solid Rogers RO4003C substrate to improve conventional C-patch input performances dedicated for radio frequency power harvesting (RFPH) application in the context of smart cities is designed. The proposed antenna can operate in the Ultra Wide Band US UWB for 5G operations, future Frequency range 3 6G (FR3 6G) operations, and the part/channels of Ku-band for future wireless applications. The comparison between the simulation and measurement results shows good agreement. The paper is organized as follows. Sections 2 and 3 present the antenna design procedure and

parametric study, respectively. Analytical approaches to calculate the input impedance and the magnetic field radiation pattern of the basic CR-patch antenna are developed in sections 4 and 5, respectively. In section 6, we show experimental results and discuss them. Section 7 gives the conclusion of the study.

II. ANTENNA DESIGN CONSIDERATIONS

In this section, design and construction processes of the studied antenna are developed. Different design steps are clearly explained in the following sub-sections.

A. GEOMETRY OF THE BASIC STRUCTURE AND WORKING MECHANISM

The proposed antenna was constructed based on the conventional planar edge-fed circular microstrip patch antenna (CMSPA/C-patch) of diameter D (in mm) as depicted in Fig. 2A. The design principles were carried out according to different design step analysis detailed as follow. Moving a part of the metallization of the conventional C-patch, the circular ring microstrip antenna (CRMSA/CR-patch) is achieved with the corresponding coordinate system, as illustrated in Fig.2B at the first step of the design procedure.

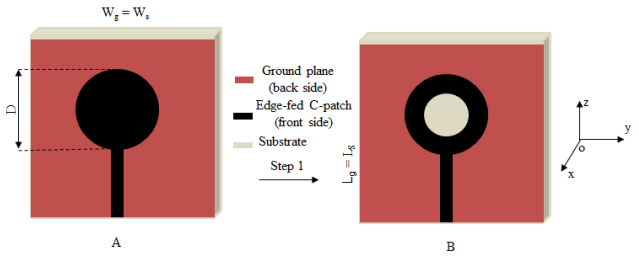

FIGURE 2. Basic structures of the studied antenna. A) conventional planar circular microstrip patch antenna (C-patch), B) planar circular ring microstrip patch antenna (CR-patch).

The proposed radiating structure is designed using the standard PCB etching technique on the front side of the 1.524-mm thick dielectric substrate RO4003C of volume $L_s \times W_s \times h$ (in mm^3). On the back side of the substrate is mounted the ground plane of area $L_g \times W_g$ (in mm^2). The designed antenna was printed using a 0.035-mm thin copper foil with an overall point-to-point size of $D \times D$ (in mm^2) in a square grid and fed by a 50-Ω microstrip transmission line. Numerical calculations of the CR-patch regarding input impedance and radiation pattern are reported in sections 4 and 5, respectively, of the present paper.

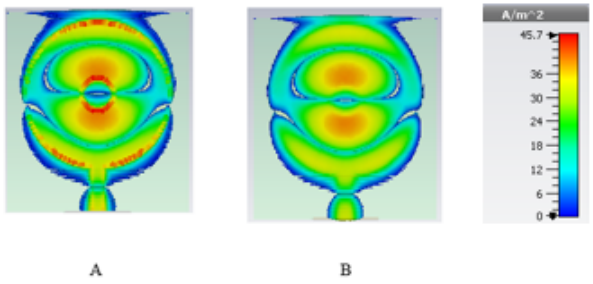

FIGURE 3. Current density propagation on the antenna at 5.8 GHz: A) Front view, B) Back view.

Fig. 3 reports the propagation current density on the studied CR-patch antenna both on the radiating element and the ground structure. The red areas around the inner edges of the ring, the edge-fed, and the opposite edge indicate a high concentration of charges and then a high area of radiation. The blue areas around the outer edges indicate a low concentration of charges responsible for radiation losses. The areas where charges are less concentrated are less significant and have a considerable impact on the efficiency, gain, directivity and bandwidth performance. The radiation zones are uniformly distributed on the radiation element and are responsible for the single band demonstrated by the conventional C-/CR-patch.

B. TRIPLE BAND OPERATION PRINCIPLE

In this section, we describe the second step of the stepwise design procedure for triple-band achievement. The goal is to produce an RFPH base-station antenna operating at multiple frequency bands using commercial software CST Microwave Studio. The studied based CR-patch antenna consists of a circular ring spread over an area of $\pi(R_2^2 - R_1^2)$ (in mm^2) where R_1 and R_2 denote the inner and the outer radii of the ring, respectively, as illustrated in Fig.4 and specified in Fig. 7.

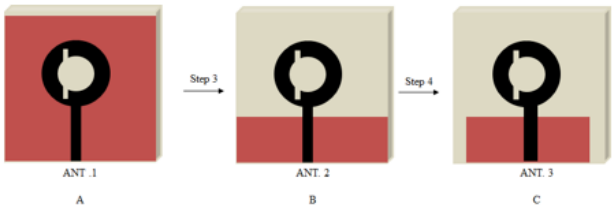

FIGURE 4. Different steps for the tri-band antenna evolution.

The geometry of the model of ANT. 1 is achieved by adding an I-shaped slot of length S_2 and width e (see Fig.7) on the CR-patch, as presented in Fig. 4a below with full ground structure at the second step of the design procedure. The full ground plane can then be considered as a reflective

structure. Indeed, the energy from the bottom surface of the loaded CR-patch passing through the dielectric was reflected back to the ground plane, which resulted in a gain enhancement (of 9.46 dB) for the initial model. The I-shaped slot acts as a capacitive load on the surface of the CR-patch, and particularly helps to control the size of achieved bandwidths. Indeed, the capacitive load aims to reduce the reflection losses between the feed line and the CR-patch, thus promoting good impedance matching. Contrarily to the previous configuration using a full ground structure at the second step of the design (model of ANT. 1), the degraded ground structure (DGS) technique is introduced in the third step to obtain the monopole-loaded CR-patch referenced as the model of ANT. 2 as depicted in Fig. 4B. The DGS creates a discontinuity between the so-formed feeding microstrip line and the CR-patch and helps to enhance the antenna performances. Hence, the degradation of the ground plane technique reduces the build-up of charges at the antenna, affecting the electric field and other characteristics such as polarization, aperture angle, and bandwidth, and creates dual-band operations, as indicated in the literature. The DGS associated with the annular ring is mainly responsible for the triple-band operation, whereas the I-shaped slot is responsible for the mismatch and bandwidth improvement. Contrarily to step 3, the DGS area is reduced as depicted in Fig. 4C in the last step of the procedure. Finally, the I-shaped slot, in conjunction with the reduced DGS area, improved of the impedance matching and desired tri-band with impressive IBW for the RFPH operations. The polarized effects of the proposed antenna are summarized in Fig. 5.

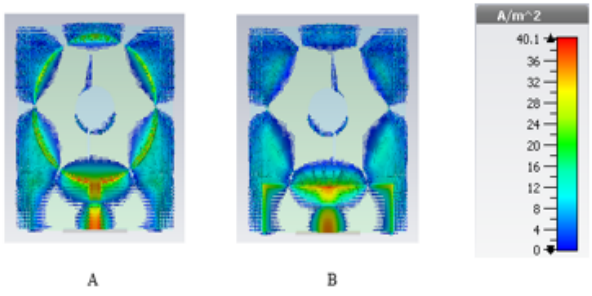

FIGURE 5. Current density distribution on the optimized ANT. 3 at 5.8 GHz: A) Front view and B) Back view.

Fig. 5 depicts the distribution of the current density both on the radiating element and on the ground structure. The degradation of the ground plane and the presence of the capacitive load on the CR-patch have modified the repartition of the charges on the antenna. It is clearly observed that the antenna is divided into six zones of radiation corresponding to the number of resonant modes observed on the input response of the optimized antenna.
All the antenna design procedures are summarized in the flow chart, as illustrated in Fig.6.

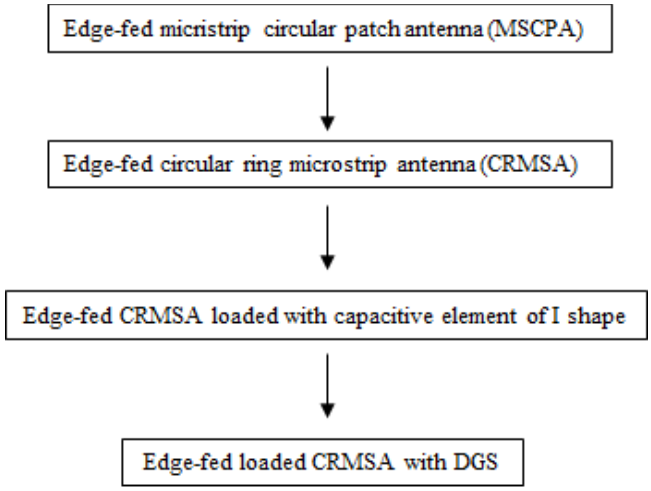

FIGURE 6. Flow chart of the proposed design.

All the antenna parameters are displayed in Fig. 7 in front and back views.

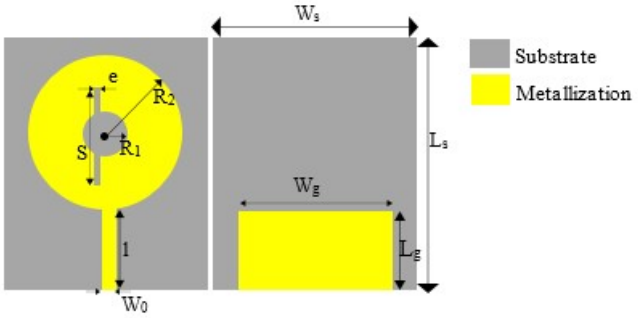

FIGURE 7. The proposed optimized antenna parameters.

The detailed geometrical optimized parameters of the proposed antenna are referred to as a model of ANT. 3 to have the best trade-off between reflection coefficients, bandwidths, and gain are summarized in Table 1 with λ_0 = 5.8 GHz.

TABLE I. Optimized antenna parameters referring to Fig. 7 nomenclature.

Antenna parameters	values (mm)
Wg	$1.64\lambda_0$
Ls	$2.36\lambda_0$
Ws	$2.08\lambda_0$
L_g	$0.65\lambda_0$
S	$1.19\lambda_0$
R_1	$0.25\lambda_0$
R_2	$0.79\lambda_0$
W_0	$0.12\lambda_0$
e	$0.04\lambda_0$

According to the antenna parameter values, the proposed antenna can be advantageously used in 5G terminals such as access points, laptops and tablets to convert EM energy into electric energy to supply the equipment of the terminals in the context of the smart or green cities.
Numerical investigation concerning the number of the capacitive load, the DGS area, and the response of model of ANT. 1, ANT. 2, and ANT. 3 are reported in the next section.

III. PARAMETRICS STUDY

Numerical investigations are realized on a lossless thin RO 4003C substrate of thickness h = 1.524 mm and, relative permittivity ε_r = 3.55 using CST Microwave Studio Simulator and the results are reported in Fig. 8.

A. INPUT PERFORMANCES

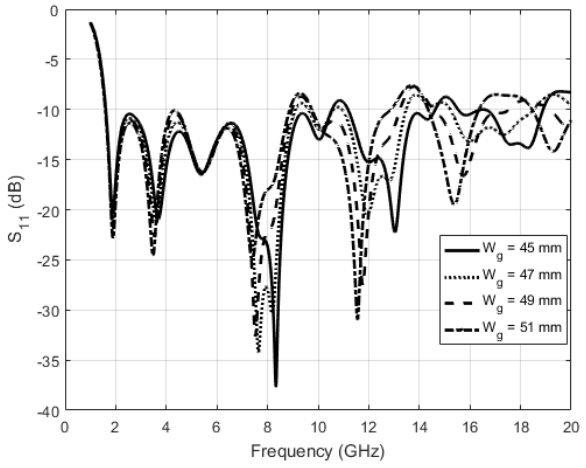

A

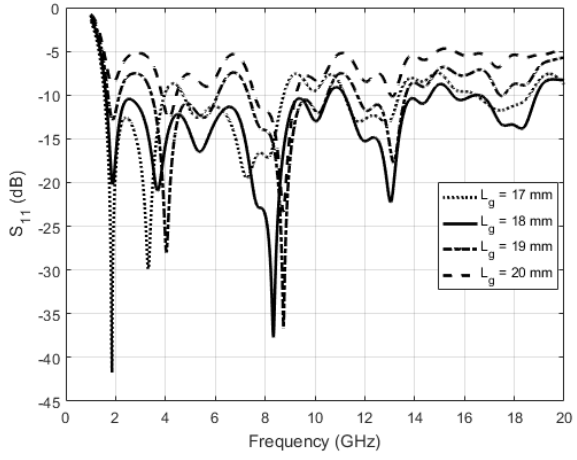

B

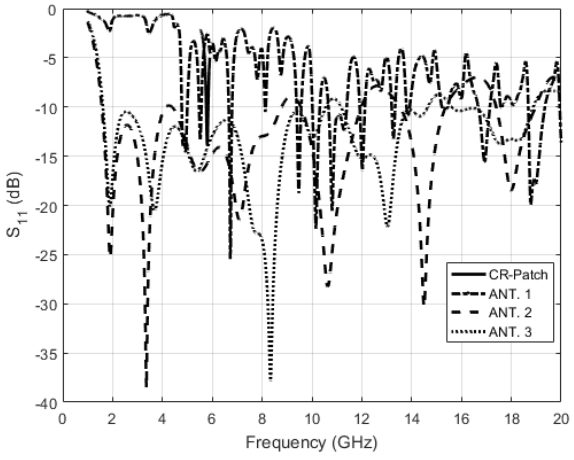

C

FIGURE 8. Simulated input performances of the proposed antenna, A) effects of ground plane length/area, B) effects of ground plane width/area, and C) optimized antennas.

Fig. 8 shows numerical experiments based on the S_{11} parameter illustrating the effects of different optimized antenna parameters in comparison of the conventional C-/CR-patch performances. It appears that DGS length has minor effects on the antenna response. Meanwhile, the DGS width has a significant impact on the resonant mode of the radiator. We can see the conventional C-patch exhibits a single mismatch narrow bandwidth whereas the designed, optimized antenna demonstrates approximately six wide bandwidths included in the major tri-band (1.608-10.550 GHz), (11.180-14.630 GHz) and (15.530-18.890 GHz) with improved impedance matching.

B. CURRENT DISTRIBUTION

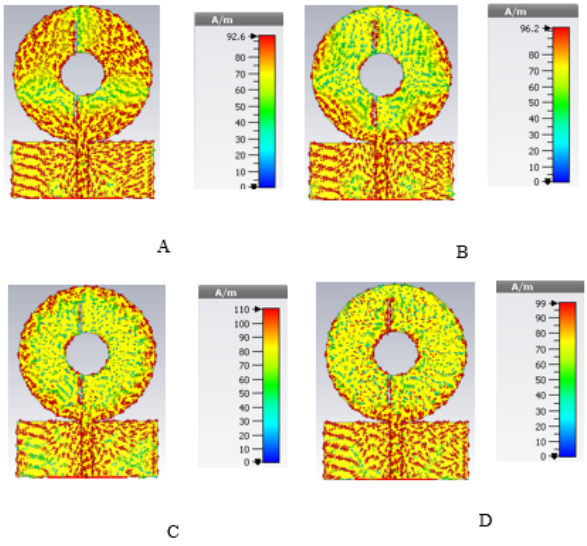

FIGURE 9. Surface current distribution for 90°-phase: A) at 4.0 GHz, B) at 5.8 GHz, C) at 12 GHz, D) at 18 GHz.

Fig. 9 demonstrates surface current distribution on the proposed optimized antenna.
Both the radiating element and the ground plane are clearly polarized. The migration of the surface currents shows that the polarization at each frequency is linear. This polarization is due to the interaction between the pulse from the RF source via the 50Ω microstrip transmission line and the circular ring surface. Based on Fig. 9 analysis, it has been observed that the lower mode of excitation is mainly due to the current concentration on the ring and on the DGS, and the intermediate mode is mainly due to the current concentration on a part of the I-shaped slot, the edge of the outer circle while the higher mode is caused by the current concentration on the I-shaped slot, the edge of the inner and the outer circle of the ring. The uniform distribution of the surface current on the loaded CR-patch significantly improves of the input and output characteristics of the single mismatch narrow bandwidth conventional C-patch.

IV. INPUT IMPEDANCE CALCULATION

Using the electromagnetic theory of the transmission line in traveling wave [26] and by considering the ring as a matched load, the expression of the input impedance of the conventional CRMSPA can be given as [16]

$$Z_{in} = Z_0 \frac{1+\Gamma_L e^{-2\gamma l}}{1-\Gamma_L e^{-2\gamma l}} \tag{3}$$

As established in [15], the input impedance of a narrow band CRMSPA is a function of its surface area through the load reflection coefficient Γ_L. If we call $\Gamma_L(S_2)$ the load reflection coefficient of the inner ring patch of surface S_2 and $\Gamma_L(S_1)$ the load reflection coefficient of the outer ring patch of the surface S_1, the reflection coefficient is determined as [15].

$$\Gamma_L = \Gamma_L(S_2) - \Gamma_L(S_1) \tag{4}$$

with

$$\Gamma_L(S_2) = \frac{Z_L - \frac{\mu_0}{4\varepsilon_0\varepsilon_r\pi^2}\left(\ln\left(\frac{R_2}{r_{moy}}\right)\right)^2}{Z_L + \frac{\mu_0}{4\varepsilon_0\varepsilon_r\pi^2}\left(\ln\left(\frac{R_2}{r_{moy}}\right)\right)^2} \tag{5}$$

$$\Gamma_L(S_1) = \frac{Z_L - \frac{\mu_0}{4\varepsilon_0\varepsilon_r\pi^2}\left(\ln\left(\frac{r_{moy}}{R_1}\right)\right)^2}{Z_L + \frac{\mu_0}{4\varepsilon_0\varepsilon_r\pi^2}\left(\ln\left(\frac{r_{moy}}{R_1}\right)\right)^2} \tag{6}$$

The load impedance can be expressed as follows: the radiating element can be considered purely inductive (the concept of modeling the radiation element to determine the value of the inductance).

$$Z_L = jL\omega \tag{7}$$

with

$$L = L_{ext} + L_{\text{int}} \tag{8}$$

Obtained from the flux calculation [16, 26, 27].

$$L_{\text{int}} = \frac{r_{moy}}{2\pi a f_r}\sqrt{\frac{2\pi\mu_0 f_r}{2\sigma}} \tag{9}$$

$$L_{ext} = \mu_0 r_{moy}\ln\left(\frac{8r_{moy}}{a} - 2\right) \tag{10}$$

with

$$r_{moy} = \frac{R_1 + R_2}{2} \tag{11}$$

$$a = \frac{R_2 - R_1}{2} \tag{12}$$

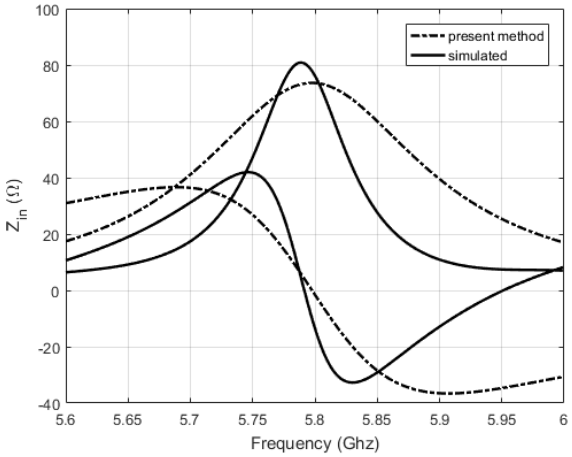

FIGURE 10. Input impedance comparison between calculation and simulation at 5.8 GHz.

Fig. 10 demonstrates the calculated and simulated input response based on the input impedance of the proposed CR-patch. All the curves are identical both demonstrating inductive and capacitive behavior at the low and high frequencies, respectively. Input resistance of around 80-Ω and input resistance bandwidth of about 4% have been achieved at the resonant frequency of 5.8 GHz. The slight difference observed between calculation and simulation curves can be explained by considering the perfect model as being purely inductive.

V. RADIATION PATTERN CALCULATION

Some EM approaches are considered in this section to evaluate radiation pattern of the basic structure. 3D or polar 2D radiation pattern is a crucial parameter that allows to characterize the antenna efficiency.

A. MAGNETIC FIELD RADIATION PATTERN

The conventional coplanar waveguide fed circular ring antenna can be treated as a circular waveguide assumed to be polarized at its surface. The simplified idea is to consider that the radiation at a spatially distant point M of a circular ring antenna can be seen as the radiation at the same spatially distant point M of the difference between two circular antenna of respective radii R_2 and R_1 (R_2 greater than R_1) identically excited at the surface. We have considered the transverse electric mode TE_{11}. Therefore, the magnetic potential vector will be determined from the polarization current density at the surface.

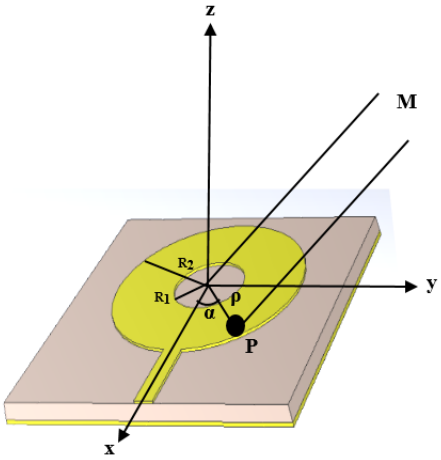

FIGURE 11. Geometry and the antenna coordinates.

The knowledge of the potential vector will allow us to find the magnetic field present in space [16].

$$R_1 \le \rho \le R_2, 0 \le \alpha \le 2\pi, 0 \le z \le h + h_a \tag{13}$$

Potential magnetic vector

$$\vec{A}(\vec{r},t) = \frac{\mu_0}{4\pi r} e^{j\omega t} e^{-jkr} \iint \vec{J}_s(\vec{\rho},\alpha) e^{jk\rho \sin\theta \cos(\alpha-\varphi)} ds' \tag{14}$$

The electric current density on the metal surface

$$\vec{J}_e(\rho,\alpha) = \vec{e}_z \wedge \vec{H}(\rho,\alpha)_{z=h+h_a} = -H_\alpha \vec{e}_\rho + H_\rho \vec{e}_\alpha \tag{15}$$

Considering a scalar electric potential $\Psi_{11}(\rho,\alpha)$ solution of the Helmholtz equation.

$$\nabla_t^2 \Psi_{1,1}(\rho,\alpha) + k_{c_{1,1}}^2 \Psi_{1,1}(\rho,\alpha) = 0 \tag{16}$$

the solution is

$$\Psi_{11}(\rho,\alpha) = J_1\left(k_{c_{1,1}}\rho\right)\cos(\alpha) \tag{17}$$

Let's put it this way and considering that the wave propagates above the top of the antenna follows the z-axis.

$$H_z(\rho,\alpha,z) = A_{1,1}\Psi_{1,1}(\rho,\alpha)\cos(\alpha) \tag{18}$$

Let's determine the transverse components of the magnetic field on the metal surface.

$$H_\alpha = A_{11}\frac{j\beta}{k_{c_{11}}^2\rho} J_1\left(k_{c_{11}}\rho\right)\sin(\alpha) e^{-\gamma z} \tag{19}$$

where $k_{c_{11}} = \frac{\chi_{11}}{R}$ the cut-off frequency, χ_{11} the zeroes of the derivative of the Bessel function and it determines the order of the resonant frequencies, and R the radius of the C-patch.

$$H_\rho = -A_{11}\frac{j\beta}{k_{c_{11}}\rho} J_1'\left(k_{c_{11}}\rho\right)\cos(\alpha) e^{-\gamma z} \tag{20}$$

The transverse components of the current densities on the metal surface are deduced.

$$J_{s\rho} = -A_{11}\frac{j\beta}{k_{c_{11}}^2\rho} J_1\left(k_{c_{11}}\rho\right)\sin(\alpha) e^{-\gamma(h+h_a)} \tag{21}$$

$$J_{s\alpha} = -A_{11}\frac{j\beta}{k_{c_{11}}\rho} J_1'\left(k_{c_{11}}\rho\right)\cos(\alpha) e^{-\gamma(h+h_a)} \tag{22}$$

We obtain this by using the relation (14), (21), and (22) and bringing back the reference in spherical coordinates.

$$A_{\varphi} = -\frac{2\pi j\tau\beta\sin(\varphi)}{k\sin(\theta)k_{c_{11}}^2} J_1\left(k_{c_{11}}R\right)J_1\left(kR\sin\left(\theta\right)\right) \tag{23}$$

with,

$$\tau = \frac{\mu_0 e^{j\omega t}e^{-jkr}}{4\pi r}\cos(\theta)e^{-\gamma\left(h+h_a\right)} \tag{24}$$

Now, we determine the second component

$$A_{\theta} = -\frac{2\pi j\xi\beta\cos(\varphi)}{k_{c_{11}}^2 - k^2\sin^2(\theta)}\left(k_{c_{11}}RJ_n\left(k_{c_{11}}R\right)A_1^{'}\right) \tag{25}$$

with,

$$A_1^{'} = J_1^{'}\left(kR\sin\left(\theta\right) - k\sin\left(\theta\right)RJ_n^{'}\left(k_{c_{11}}\right)J_1\left(kR\sin\left(\theta\right)\right)\right)$$
$$\xi = \frac{\mu_0 e^{j\omega t}e^{-jkr}}{4\pi r k_{c_{1,1}}^2}e^{-\gamma\left(h+h_a\right)} \tag{26}$$

We know from Faraday that the magnetic field is rotational.

$$\vec{B}(\vec{r},t) = \vec{\nabla}\wedge\vec{A}(\vec{r},t) \tag{27}$$

After transformation, we see that the field only varies the potential vector along the radial component. We can, therefore, generalize the expression of the transverse components of the magnetic field vector.

$$B_{\theta} = jkA_{\varphi} \tag{28}$$

$$B_{\varphi} = -jkA_{\theta} \tag{29}$$

Assuming the principle of superposition, we can deduce the radiated field at a great distance by differentiating the magnetic fields obtained from surfaces of different radii. Hence,

$$B_{\theta}(ring) = B_{\theta}(S_2) - B_{\theta}(S_1) \tag{30}$$

$$B_{\varphi}(ring) = B_{\varphi}(S_2) - B_{\varphi}(S_1) \tag{31}$$

with $S_2(O,R_2)$, $S_1(O,R_1)$ and $R_1 < R_2$

B. RADIATION PATTERN PLOT

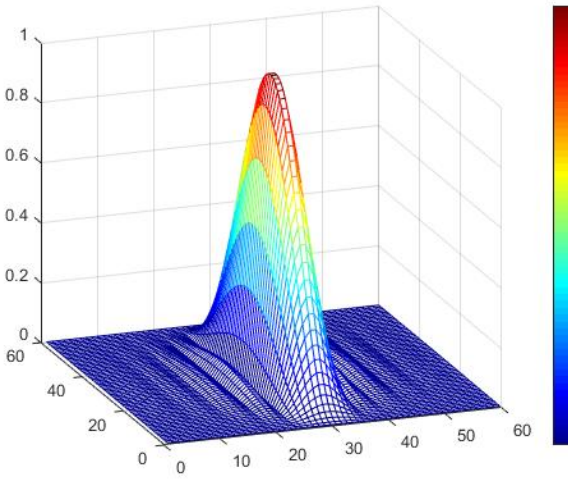

A

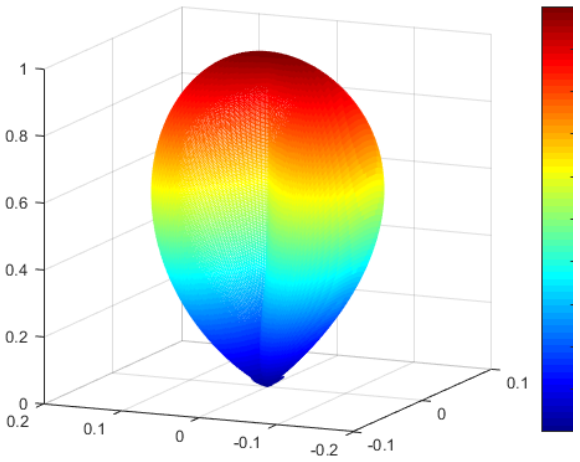

B

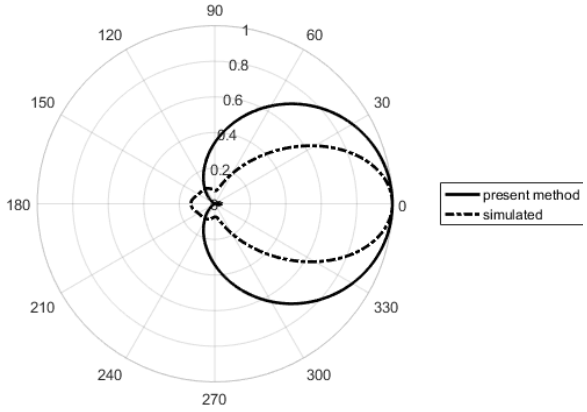

C

FIGURE 12. Magnetic field radiation patterns: A) Cartesian 3D; B) polar 3D, C) polar Cartesian.

Fig. 12 shows the normalized magnetic field radiation pattern in the scalar scale of the CR-patch obtained by calculation regarding the resonant cavity method elaborated in the previous section for $\chi_{11} = 1.841$, $\lambda = 0.0281$ m and $k = 223.3289$ rad/m. The proposed antenna radiates uni-directionally in the direction perpendicular to the radiating element with a half-power beamwidth (HPBW) of about 90° as expected [18]. The absence of the side lobes can be explained by the choice of the calculation method on one hand and the value of the external radius in relation to the wavelength on the other hand. The cavity method considers the antenna as a surface-polarized block and not as a superimposed stratified layer. To this end, the calculation of the magnetic field does not consider intrinsic properties that could greatly influence the radiation through the antenna, such as the thermal constant, the loss tangent, the diffusivity, the discontinuity caused by the presence of current density between layers of different dielectric constants.

VI. EXPERIMENTAL RESULTS AND DISCUSSION

The optimized prototype of the proposed antenna has been fabricated on a thin Rogers 4003C substrate of relative permittivity ε_r = 3.55, thickness h = 1.524 mm, and loss tangent 0.0027 (tanδ = 0.0027). Its overall volume is 64.8×57×1.524 (in mm^3), whereas the circular ring spread over an area of 1338.4 mm^2. The photograph of the fabricated antenna is shown in Fig. 13 and the input performances based on input reflection coefficient are depicted in Fig. 14.

A. TEST SETUPS

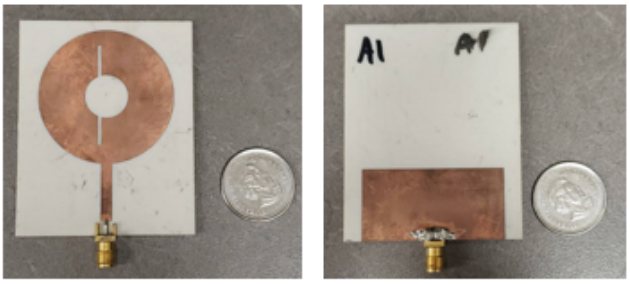

A B

FIGURE 13. The hardware prototype of the proposed antenna: A) Front view; B) Back view.

B. TEST RESULTS

The results obtained from the hardware prototype of the proposed design are presented and compared with the simulation results. Commercial software CST Microwave Studio is used for numerical experiments whereas vector network analyzer (VNA) is used to measure antenna input characteristics.

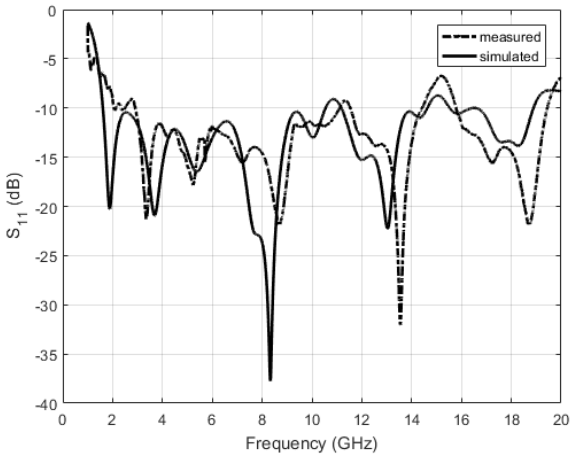

FIGURE 14. Measurements and simulations based on the input reflection coefficient of the fabricated antenna.

Fig. 14 shows the measured and simulated input reflection coefficient vs frequency of the fabricated antenna. Experimentally, it is clearly observed that the proposed antenna can be used satisfactorily to collect RF energy in three different frequency ranges. The lower band (2.980-11.110 GHz) is centered at the frequency 4.63 GHz with an impressive 142% FBW (193% respectively for simulation) which can be used in US UWB for UWB applications. The middle band (11.540-14.420 GHz) with resonant frequency 13.03 GHz with 21.3% FBW (respectively for simulation) can be used for 5G mmW operations, US Direct Broadcast Satellite (12.2-12.7 GHz)/(11.7-12.5 GHz) and also

deployed for future FR3 band for 6G operations. The upper band (15.780-19.440 GHz) centered at the frequency 18.26 GHz with 19.6% FBW (respectively for simulation) which can be considered as a section of the Ku-band and then can also be allocated for future FR3 band for 6G operations. The comparison of the studied antenna performances in the three frequency bands obtained between measurements and simulations is reported in Table 2. Lower frequency (F_L), higher frequency (F_H), resonant frequency (F_r), and FBW are considered as parameters for Table 2.

TABLE II. COMPARATIVE PERFORMANCES OF THE PROPOSED DESIGN BY MEASUREMENTS AND SIMULATIONS

Frequency band	Simulations/ Measurements			
	F_L (GHz)	F_H (GHz)	F_r (GHz)	FBW (%)
Lower band	1.608/ 2.980	10.550/ 11.110	4.630/ 5.730	193/ 142
Middle band	11.180/ 11.540	14.630/ 14.420	13.030/ 13.550	26.5/ 21.3
Upper band	15.530/ 15.780	18.890/ 19.440	18.260/ 18.690	18.4/ 19.6

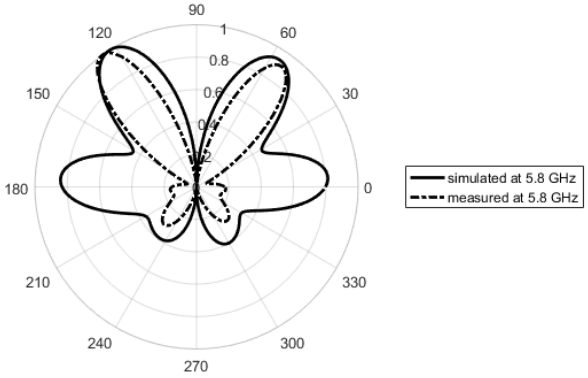

A

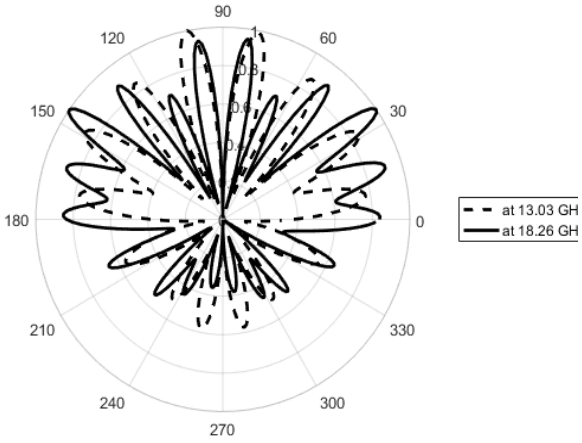

B

FIGURE 15. Output performance of the proposed antenna, A) magnetic field radiation pattern in xz-plan, simulated and measured at 5.8 GHz B) magnetic field radiation pattern in xz-plan, simulated at 13.03 GHz and 18.26 GHz.

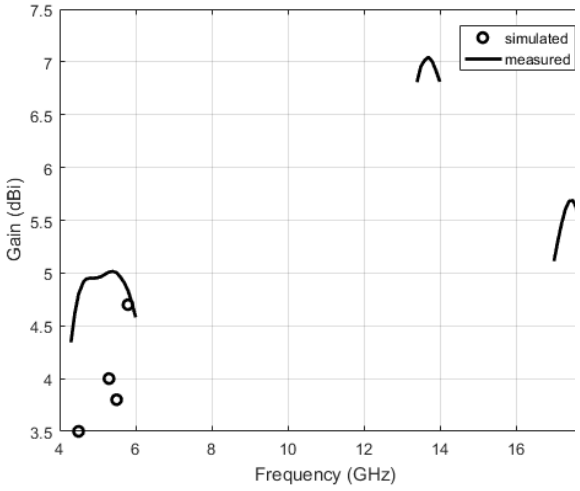

FIGURE 16. Output performances of the proposed antenna, simulated gain and measured gain.

Fig. 15 depicts the output responses of the proposed design antenna. It can be noted that the radiation pattern of the proposed antenna is bi-directional. It appears several main lobes with high level in the broadside direction exhibiting half-power beam-width (HPBW) of about 85° and neglected side lobe level. In the Figure 16, a single measured peak gain of 4.2 dBi at 5.8 GHz has been obtained due to the limitation of the measurement setup. We also observe the obtained gain maesured at 3.5 dBi for 4.5 GHz, 4 dBi for 5.3 GHz and 3.8 dBi for 5.5 GHz. Conversely simulated real stable maximum gain achieved is

5.016 dBi, 7.046 dBi, and 5.687 dBi at the resonant frequencies of 5.4 GHz, 13.7 GHz, and 17.5 GHz, respectively.

C. DISCUSSION

Calculation of the input impedance using the transmission line method and considering the circular geometry of the antenna gave a fairly satisfactory result, which could be verified in simulation at 5.8 GHz using suitable simulation software. Similarly, thanks to the superposition method, we were able to establish the equation for the components of the magnetic field using the resonant cavity method. Measured results are in good accordance with simulated results except in a few instances. The slight difference between simulated and measured results may be due to the fabrication loss, connector loss and tolerance in dielectric constant, high mode excitation, the losses due to the coaxial feed/connector, the manual positioning, the environment of the experiment, measurement conditions, etc. By modifying the geometry of the conventional CR-patch, and impressive improvement of the single mismatch narrow bandwidth of the conventional C-patch was achieved.

A comparative study between the present work and the published triple-band antenna designs is given in Table 3. Operating frequency band (OFB), resonant frequency (F_r), and FBW are considered as parameters for Table 3.

TABLE III. COMPARATIVE MEASURED RESULTS OF THE PROPOSED ANTENNA AND PUBLISHED DESIGNS.

Ref	Frequency	Fr (GHz)	FBW (%)	Gain (dBi)	size of design (mm^3)
	Wi-Fi (2.4-2.51GHz)	2.445	4.49	2.72	
[8]	ISM (5.13-5.86GHz)	5.85	12.48	3.6	15x12x1.6
	X-Band (7.7-9.53GHz)	8.83	20.72	4.4	
	5G Cellular	3.5	0.05	NA	
[9]	5G Wi-Fi	5.5	0.1	NA	16x10x1.6
	Wi-Fi 6	6.5	0.1	NA	
	SUB-6G	2.42	5.1	0.64	
[10]	WLAN	3.7	16.6	1.21	
	WIMAX	5.7	23.7	1.81	30x17x1.6
	C-Band	5.5	<0.1	1.7	
[14]	C-Band	6.6	<0.1	2.5	
	X-Band	10.4	<0.1	3.2	20x22x1.5
	LoRaWAN	0.85	0.8	4.56	
[22]	GSM 1800MHz	1.85	9.2	2.95	
	UMTS 2,1GHz	1.95	11.9	1.38	103.41x80.29x1.6
	LTE (0.79-0.96GHz)	0.9	11.0	1.3	
[23]	LTE (1.71-2.17GHz)	2.0	20.5	2.3	
	LTE (2.5-2.69GHz)	2.69	14.3	6.0	110x110
	Wi-Fi 2.4GHz	2.4	10.0	4.2	
[24]	Wi-Fi 5GHz	4.0	10.0	4.42	
	C-band	5.0	15.0	4.42	60x60x1.6
	C-band 5.42GHz	5.42	4.6	6.6	
	C-band 6.9GHz	6.9	2.9	7.3	40x40x0.8
[25]	C-band 7.61GHz	7.61	3.3	7.1	
	GSM 900MHz	0.92	4.2	8.15	
	GSM 1800MHz	1.84	1.7	7.1	84x35x1.6
[28]	UMTS 2100MHz	2.1	1.0	8.15	
	UMTS 2100MHz	2.0	9.0	7.0	
	Wi-Fi 2.4GHz	2.5	29.0	5.5	72x68x1.6
[29]	WIMAX	3.0	30.0	9.2	
	US UWB (2.98-11.11GHz)	4.63	142.0	4.94	
	US DBS (11.54-14.42GHz)	13.03	21.3	6.35	64.8x57x1.524
This Work	FR3 6G (15.78-19.44GHz)	18.26	19.6	5.26	

We can see that our proposed antenna offers one impressive bandwidth and two wider frequency bands than [9], [14], [22], [23], [24], and [25]. We can see from the simulation data that the gains achieved in work are smaller than those proposed in [25], [28] and [29] but much larger than those proposed in [8], [10], [14], [25], and [29] with competitive size. The gain values observed in our antenna are suitable for RF power conversion systems.

VII. CONCLUSION

A compact, low profile I-shaped slot-loaded triple-band monopole CR-patch to improve conventional C-patch input performances for RF energy harvesting applications has been introduced. Calculation methods to evaluate input and output performances of the basic structure based on the C-patch antenna have been developed. Numerical experiments using CST microwave studio suite show that the proposed

antenna operates suitably in the US UWB band for UWB applications (2.98-11.11 GHz), US DBS/FR3 band for IoT, and Ku-band/FR3 band for 6G operations (11.54-14.42 GHz), and (15.78-19.44 GHz). The performances of the prospective radiator are assessed through numerical and experimental investigation. The multi-band proposed antenna then covers 5.8 GHz, corresponding to 5G and the above-mentioned standards, suitable for RF power harvesting applications in smart cities. Experimentally, the prospective radiator demonstrates excellent impedance matching bandwidths (IBW) performance at 4.63 GHz, 13.03 GHz, and 18.26 GHz with minimum input reflection coefficient -21.62 dB, -31.8 dB, and -21.6 dB. The measured FBWs are about 142%, 21.3%, and 19.6% respectively. Numerical and experimental results regarding input and output performances obtained make the proposed design antenna an excellent candidate for present and future wireless communication systems in conjunction with RF energy harvesting applications. To achieve our objectives consisting to design novel rectenna, the next product will focused on the implementation of the rectifier circuit using the proposed UWB antenna to accomplish the harvested RF energy requirements.

REFERENCES

[1] N. A. Moghaddam, A. Maleki, M. Shirichian, and N. S. Panah, "RF energy harvesting system and circuits for charging of wireless devices using spectrum sensing," in *2017 24th IEEE International Conference on Electronics, Circuits and Systems (ICECS)*, 2017: IEEE, pp. 431-436.

[2] L.-G. Tran, H.-K. Cha, and W.-T. Park, "RF power harvesting: a review on designing methodologies and applications," *Micro and Nano Systems Letters,* vol. 5, pp. 1-16, 2017.

[3] D. Potti, G. N. A. Mohammed, K. Savarimuthu, S. Narendhiran, and G. Rajamanickam, "An ultra-wideband rectenna using optically transparent Vivaldi antenna for radio frequency energy harvesting," *International Journal of RF and Microwave Computer-Aided Engineering,* vol. 30, no. 10, p. e22362, 2020.

[4] A. M. Jie, N. Nasimuddin, M. F. Karim, and K. T. Chandrasekaran, "A dual-band efficient circularly polarized rectenna for RF energy harvesting systems," *International Journal of RF and Microwave Computer-Aided Engineering,* vol. 29, no. 1, p. e21665, 2019.

[5] M. A. Shukoor, V. Kumar, and S. Dey, "Compact polarisation insensitive wide angular stable triple band absorber for RF energy harvesting, RCS reduction, and sensor applications," *International Journal of RF and Microwave Computer-Aided Engineering,* vol. 31, no. 9, p. e22763, 2021.

[6] P. Das and A. Karmakar, "A reconfigurable wideband MIMO antenna combines RF energy harvesting," *International Journal of Communication Systems,* p. e5683, 2024.

[7] A. Varshney and D. N. Gençoğlan, "Offset-fed Slotted Antenna Practically Loaded with Split Ring as Water Quality Sensor for X-Band Industrial Applications," *Advanced Electromagnetics,* vol. 13, no. 2, pp. 39-52, 2024.

[8] S. Angadi, K. Viswanadha, R. Chinthaginjala, C. Dhanamjayulu, K. Tai-hoon, and S. Kumar, "Meta-atom loaded circularly polarized triple band patch antenna for Wi-Fi, ISM and X-band communications," *Heliyon,* 2024.

[9] A. Ali *et al.*, "A compact mimo multiband antenna for 5g/wlan/wifi-6 devices," *Micromachines,* vol. 14, no. 6, p. 1153, 2023.

[10] L. Kumar, V. Nath, and B. Reddy, "Triple-band stub loaded patch antenna with high gain for 5G Sub-6 GHz, WLAN and WiMAX applications using DGS," *Facta Universitatis, Series: Electronics and Energetics,* vol. 36, no. 2, pp. 171-188, 2023.

[11] X. Lu, P. Wang, D. Niyato, D. I. Kim, and Z. Han, "Wireless networks with RF energy harvesting: A contemporary survey," *IEEE Communications Surveys & Tutorials,* vol. 17, no. 2, pp. 757-789, 2014.

[12] D. N. Elshaekh, H. A. Mohamed, H. A. Shawkey, and S. I. Kayed, "Printed circularly polarized split ring resonator monopole antenna for energy harvesting," *Ain Shams Engineering Journal,* vol. 14, no. 6, p. 102182, 2023.

[13] Y. C. Lee *et al.*, "High-Performance Multiband Ambient RF Energy Harvesting Front-End System for Sustainable IoT Applications-A Review," *IEEE Access,* 2023.

[14] A. K. Nghaimesh and A. K. Jassim, "Triple-Band Circular Patch Microstrip Antenna for Wireless Communication," *Journal of Engineering and Sustainable Development,* vol. 28, no. 1, pp. 64-74, 2024.

[15] C. Mbinack, E. Tonye, and D. Bajon, "Microstrip-line theory and experimental study for the characterization of the inset-fed rectangular microstrip-patch antenna impedance," *Microwave and optical technology letters,* vol. 57, no. 2, pp. 514-518, 2015.

[16] C. A. Balanis, *Antenna theory: analysis and design*. John Wiley & sons, 2015.

[17] K. Mondal, B. Bag, and P. P. Sarkar, "Axial ratio bandwidth improvement of compact planar monopole antenna with dual-band and dual-sense," *International Journal of Communication Systems,* vol. 37, no. 5, p. e5688, 2024.

[18] R. Bodo, C. Mbinack, J. S. A. Eyébé Fouda, and E. Tonye, "Duo triangle-shaped rectangular microstrip-fed patch antennas input and output parameters investigation," *International Journal of*

Circuit Theory and Applications, vol. 47, no. 7, pp. 1057-1070, 2019.

[19] Y.-J. Ren, M. F. Farooqui, and K. Chang, "A compact dual-frequency rectifying antenna with high-orders harmonic-rejection," *IEEE Transactions on Antennas and Propagation,* vol. 55, no. 7, pp. 2110-2113, 2007.

[20] K. Niotaki, S. Kim, S. Jeong, A. Collado, A. Georgiadis, and M. M. Tentzeris, "A compact dual-band rectenna using slot-loaded dual band folded dipole antenna," *IEEE Antennas and Wireless Propagation Letters,* vol. 12, pp. 1634-1637, 2013.

[21] M. F. Shaker, H. A. Ghali, D. M. N. Elsheakh, and H. A. E. Elsadek, "Multiband coplanar monopole antenna for energy harvesting," in *2018 IEEE international symposium on radio-frequency integration technology (RFIT)*, 2018: IEEE, pp. 1-3.

[22] A. D. Boursianis *et al.*, "Triple-band single-layer rectenna for outdoor RF energy harvesting applications," *Sensors,* vol. 21, no. 10, p. 3460, 2021.

[23] V. Palazzi *et al.*, "A novel ultra-lightweight multiband rectenna on paper for RF energy harvesting in the next generation LTE bands," *IEEE Transactions on Microwave Theory and Techniques,* vol. 66, no. 1, pp. 366-379, 2017.

[24] M. Saravanan and A. Priya, "Design of tri-band microstrip patch rectenna for radio frequency energy harvesting system," *IETE Journal of Research,* vol. 68, no. 4, pp. 2410-2415, 2022.

[25] N. Singh, B. K. Kanaujia, M. T. Beg, T. Khan, and S. Kumar, "A dual polarized multiband rectenna for RF energy harvesting," *AEU-International Journal of Electronics and Communications,* vol. 93, pp. 123-131, 2018.

[26] D. M. Pozar, *Microwave Engineering*, fourth ed. p. 756.

[27] J. L. Dion, L. Dion, Ed. *Électromagnétisme Phénomènes d'induction*, 2002, p. 420.

[28] S. Shen, C.-Y. Chiu, and R. D. Murch, "A dual-port triple-band L-probe microstrip patch rectenna for ambient RF energy harvesting," *IEEE Antennas and Wireless Propagation Letters,* vol. 16, pp. 3071-3074, 2017.

[29] S. Chandravanshi, S. S. Sarma, and M. J. Akhtar, "Design of triple band differential rectenna for RF energy harvesting," *IEEE Transactions on Antennas and Propagation,* vol. 66, no. 6, pp. 2716-2726, 2018.